

A Composite of Nb₂O₅ and MoO₂ as a High-Capacity High-Rate Anode Material for Lithium-Ion Batteries

Evangeline C. Wheeler-Jones,^[a] Melanie J. Loveridge,^{*[a]} and Richard I. Walton^{*[b]}

A composite of Nb₂O₅ and MoO₂ was synthesised using a hydrothermal reaction (225 °C) followed by a short heat-treatment step (600 °C) to achieve a high-capacity, high-rate anode for lithium-ion battery applications. The composite was shown via powder X-ray diffraction and electron microscopy to be an intimate mix of individual oxide particles rather than an atomically mixed oxide material, and shown by X-ray fluorescence spectroscopy (XRF) to contain a 45:55 ratio of

Nb:Mo. This material is demonstrated to show notable rate capability in lithium (Li) half-cell cycling and rate tests. When cycled at 100 °C the material achieved over 100 mAh g⁻¹ even after 400 cycles and shows a stable reversible capacity of 514 mAh g⁻¹ (at 1 C), realising its theoretical capacity. The composite shows electrochemical results comparable to Nb₂O₅; C composites yet achieves far higher capacities at low-rate due to the MoO₂ content.

Introduction

Metal oxides have been comprehensively investigated as anode materials for lithium-ion batteries (LIBs) due to their diverse chemistry and breadth of properties.^[1–9] Amongst these, Nb₂O₅ is of particular interest due to its unique intercalation pseudocapacitive properties, hence its application as a high-rate anode.^[10–14] Nb₂O₅ has a reasonable capacity (200 mAh g⁻¹, described by $\text{Nb}_2\text{O}_5 + x\text{Li}^+ + xe^- \leftrightarrow \text{Li}_x\text{Nb}_2\text{O}_5$, when $x=2$)^[15,16] but would struggle to compete with high capacity materials such as Si, since, as with many oxides, Nb₂O₅ is limited by its conductivity.^[17] MoO₂ is a rare oxide that is both conductive and has a high capacity towards lithium (838 mAh g⁻¹, four electron reaction),^[18–21] where the four-electron reaction is achieved via a Li-ion storage mechanism which is a combination of conversion and intercalation.^[22] However, due to the nature of the conversion reaction MoO₂ lacks long term stability, or high-rate capability. Both of these oxides have been investigated previously to understand their ion storage mechanisms and to optimise their beneficial properties.^[21,23–25]

A common approach to improve lithium insertion in oxides is to fabricate a composite with carbon. In the case of Nb₂O₅ this aims to improve its conductivity, whereas for MoO₂ it is used as a matrix to stabilise the material.^[26–31] This type of work has led to the formulation of composites using a combination of promising

anode materials, rather than using carbon alone, to further broaden the materials' electrochemical properties.^[32–40] Notably, Kim *et al.* developed nano-clusters made of Nb₂O₅ and Ge/GeO₂, to boost conductivity.^[41] This study compared the composite electrochemically to a physically mixed version, and the composite showed higher capacities, demonstrating the intimate mixing between these materials as key to achieving the desired electrochemical properties. Similarly, Wang *et al.* combined MoO₂ and Mo to produce improved stabilities and capacities of 570 mAh g⁻¹ at 4.0 A g⁻¹.^[42] These results were linked to the increased metallic Mo availability to contribute a reversible conversion process in MoO₂ which was achieved due to the composite formulation.

In this paper we describe an experimental study that looks to combine MoO₂ and Nb₂O₅ in a composite. This produces a material that integrates the favourable properties of the individual oxides towards lithium insertion, whilst negating unfavourable properties.

Results

Hydrothermal synthesis yielded an as-synthesised composite with an XRD pattern which could be assigned as a combination of monoclinic MoO₂ and anisotropically crystalline Nb₂O₅ (Figure S1).^[43] The as-synthesised composite pattern has very broad features which are attributed to the semi-crystalline nature of the Nb₂O₅, with key Bragg peaks at 22° and 46° from the (001) and (002) planes, respectively, assuming the form is a structure related to T-Nb₂O₅ (Figure 1).^[43] Alongside this are broad peaks matched to the monoclinic MoO₂ suggesting a small crystalline size or poor crystallinity. There appear to be no other peaks that can be attributed to a crystalline mixed oxide phase, suggesting a successful composite formation. The composite was heat-treated to 600 °C with the aim to form the expected T-Nb₂O₅ phase, yet the XRD pattern shows very little change (Figure 1). There appears to be no formation of new phases, but there is a sharpening of the peaks and flattening of the broad regions. This suggests an improvement in crystallinity, however there is no obvious

[a] E. C. Wheeler-Jones, Dr. M. J. Loveridge
University of Warwick
Coventry, CV4 7AL (UK)
E-mail: M.Loveridge@warwick.ac.uk

[b] Prof. R. I. Walton
Department of Chemistry
University of Warwick
Coventry, CV4 7AL (UK)
E-mail: r.i.walton@warwick.ac.uk

 Supporting information for this article is available on the WWW under <https://doi.org/10.1002/batt.202200556>

 © 2023 The Authors. *Batteries & Supercaps* published by Wiley-VCH GmbH. This is an open access article under the terms of the Creative Commons Attribution License, which permits use, distribution and reproduction in any medium, provided the original work is properly cited.

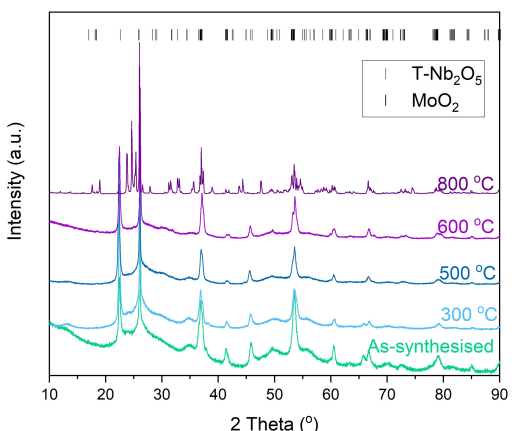


Figure 1. XRD patterns of the $\text{Nb}_2\text{O}_5:\text{MoO}_2$ composite, after increasing temperatures of heat-treatment to 800°C , heated for 4 h in Ar.

formation of T- Nb_2O_5 as would be expected.^[44] The main peaks present in the T-phase are already seen in the semi-crystalline form, however other intense peaks for example, at $\sim 28^\circ$, do not appear (Figure S2). This suggests that the Nb_2O_5 has suppressed crystallinity and may still be semi-crystalline even with heat-treatment. This may be due to the presence of the MoO_2 particles inhibiting the growth of the T- Nb_2O_5 phase, thus this composite may be exhibiting Zener pinning, where one set of particles constrains the other restricting further grain growth.^[45,46] Further heat-treatment to 800°C was trialled to establish whether the T-phase could be produced at higher temperatures, and yet here monoclinic $\text{Nb}_2\text{O}_5\cdot(\text{H}_2\text{O})$ was formed alongside monoclinic MoO_2 and $\text{Mo}_{13}\text{O}_{33}$ (Figure S3).^[47–49] Therefore, as the 600°C material only

consists of Nb_2O_5 and MoO_2 , and appears to have improved crystallinity versus the other temperature it was taken forward for further investigation.

XRF was used to confirm the ratios of the metals within the composite, where a slightly higher Mo content than anticipated was achieved: Nb of 44.8 ± 0.4 atm %, with 55.2 ± 0.4 atm % of Mo. These ratios were unchanged between heat-treated and as-synthesised materials. XPS results show Mo^{4+} screened and unscreened state typical of the orbital splitting seen in MoO_2 (Figure 2a). Mo^{6+} states are also observed potentially suggesting there are areas of Mo in a further oxidised state, likely to be that at the surface of the MoO_2 particles. The Nb state sits in a +5 state with a Nb 3d–O 1s difference of 323.65 eV, which is typical for +5 niobates, expected at ~ 323.5 eV.^[50] These results are very typical for the oxides and suggest that the composite is an intimate mix of separate oxide particles rather than a substituted or mixed oxide form. In addition, the presence of C, N and O signals on the surface show that the heat-treatment may not have removed the surface species on the material from the hydrothermal synthesis process (Figure 2b–d). This maybe expected due to the morphology and complex mixing of particles, which may make complete removal of these species particularly difficult.

The SEM images show agglomerates of nanoparticles with undefined morphologies, yet the EDX mapping reveals distinct Mo and Nb rich particles which are interspersed in the sample (Figure 3a, b). TEM reveals that the agglomerates are in the form of high aspect ratio nanowires and near spherical particles intimately mixed (Figure 3c). It is expected that the nanowires are Nb_2O_5 based on our previous work on these materials,^[43] and STEM-EDX confirms this (Figure 3d). When compared to the as-synthesised material, heat-treatment caused MoO_2 primary par-

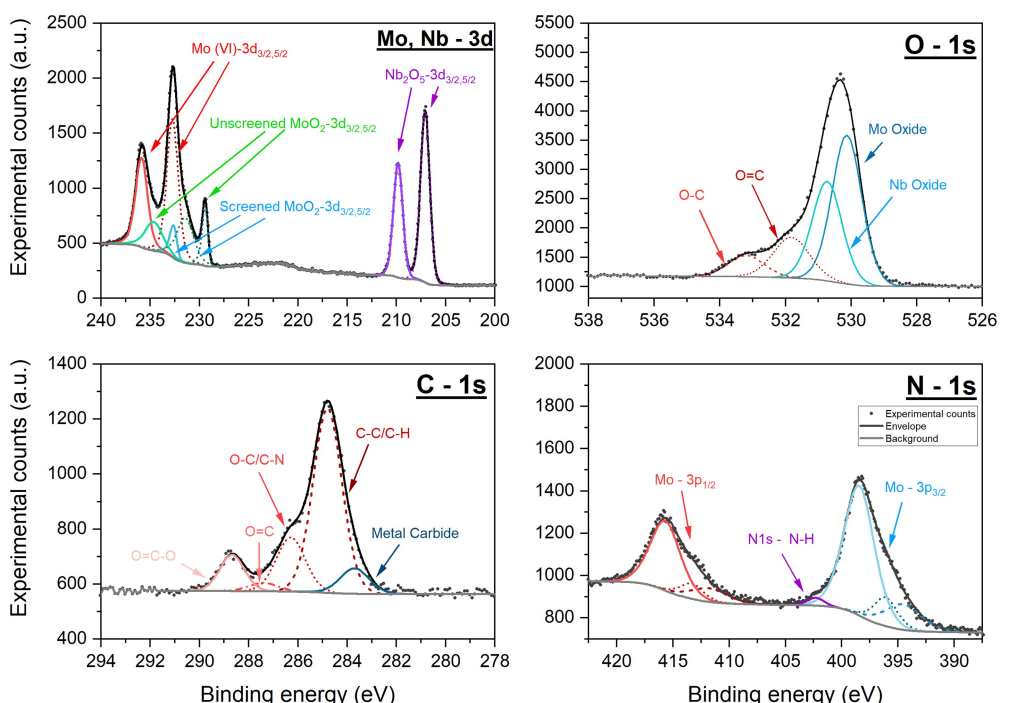


Figure 2. High resolution XPS spectra of a) the Mo and Nb 3d region, b) O 1s region, c) C 1s region and d) N 1s region for the $\text{Nb}_2\text{O}_5:\text{MoO}_2$ composite. The full scan is provided in Figure S4.

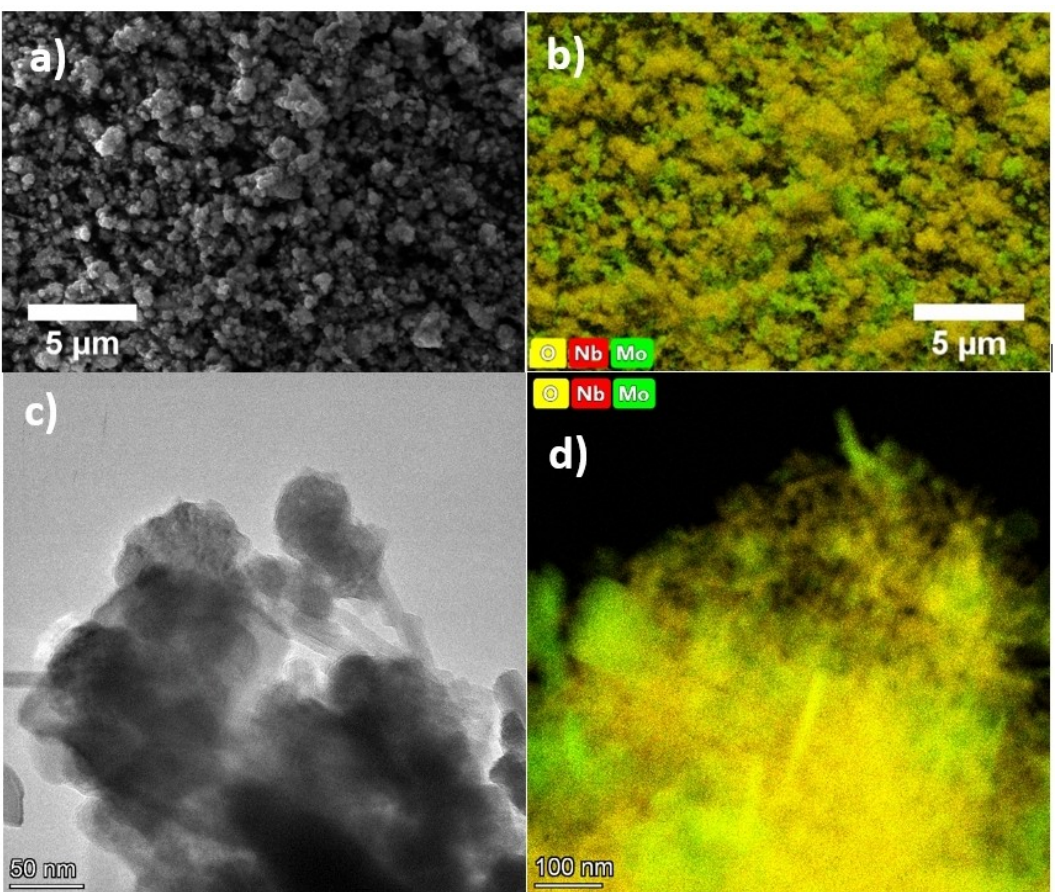


Figure 3. a) SEM image, b) SEM-EDX map, c) TEM image, d) STEM-EDX map of the $\text{Nb}_2\text{O}_5:\text{MoO}_2$ composite where maps show Mo in green, Nb in red and O in yellow.

ticles to fuse together (Figure S5). Regarding the Nb_2O_5 particles, the morphology does not change with increasing temperature, consistent with the lack of T- Nb_2O_5 phase formation in the XRD pattern. This suggests that these materials exist in the same form, and the presence of MoO_2 at this quantity suppresses crystallisation due to Zener pinning.

The composite was investigated as an anode vs Li in a 0.01–3.0 V window, and all cells were subjected to a C/20 formation prior to cycling. The C-rate is calculated using a theoretical capacity of 519 mAh g⁻¹ which is calculated from the ratio of Nb_2O_5 and MoO_2 and their respective capacities of 200 and 838 mAh g⁻¹. The lithiation appears reversible with good capacity retention, where at 200 cycles an average capacity of 514 mAh g⁻¹ is recorded (at 1 C), which reaches the theoretical capacity. During cycling, there is an initial loss in capacity from SEI formation before a subsequent increase between 10 and 30 cycles (Figure 4); this appears to be the activation process typical of MoO_2 (Figure S6).^[51] It can also be noted that that initial capacity of pure Nb_2O_5 exceeds the theoretical capacity (Figure S6): this has been reported by others and ascribed to oxide deficient stacking faults in disordered forms of the material.^[52] Following this, there is additional loss in capacity until 60 cycles, where the capacity increases again. This is due to a multi-stage activation process, the further characterisation of which is discussed below.

Regarding current (rate), when the C-rate is increased from C/5 to 1 C, the capacity results are remarkably similar even over 200 cycles (Figure 4). As may be expected with further rate increase, there is a larger drop in capacity as at this rate not all Li can be inserted or removed from the anode. The trend in capacity with cycle number remains at 5 C but at 20 C the hump shape of the activation process appears flattened, and the second activation is not obvious. At 100 cycles, the average capacities are 480, 492, 301 and 165 mAh g⁻¹ for C/5, 1 C, 5 C and 20 C, respectively. All charge profiles appear almost linear, with a slight inflection at ~1.0 V, which may suggest a phase transition. This type of slope, with lack of clear plateau suggests a solid-solution Li-ion insertion mechanism. Although there is a loss in capacity between 1 C and 20 C, this is in line with work by Liu *et al.*, one of the few studies that presented high-rate results for a pure MoO_2 .^[53] The capacities also surpass recent work reported on pure Nb_2O_5 ,^[54–56] which is expected due to its lower theoretical capacity. There appears to be some polarisation at this rate, suggesting further work is needed to improve the resistance at high rates via routes such as optimisation of the slurry formulation and the electrode manufacturing route.

Cyclic voltammetry was used to help identify the mechanism of Li-ion storage (Figure 5a). The CV shows three pairs of redox peaks: during lithiation at 1.5, 1.25 and 0.2 V, and during

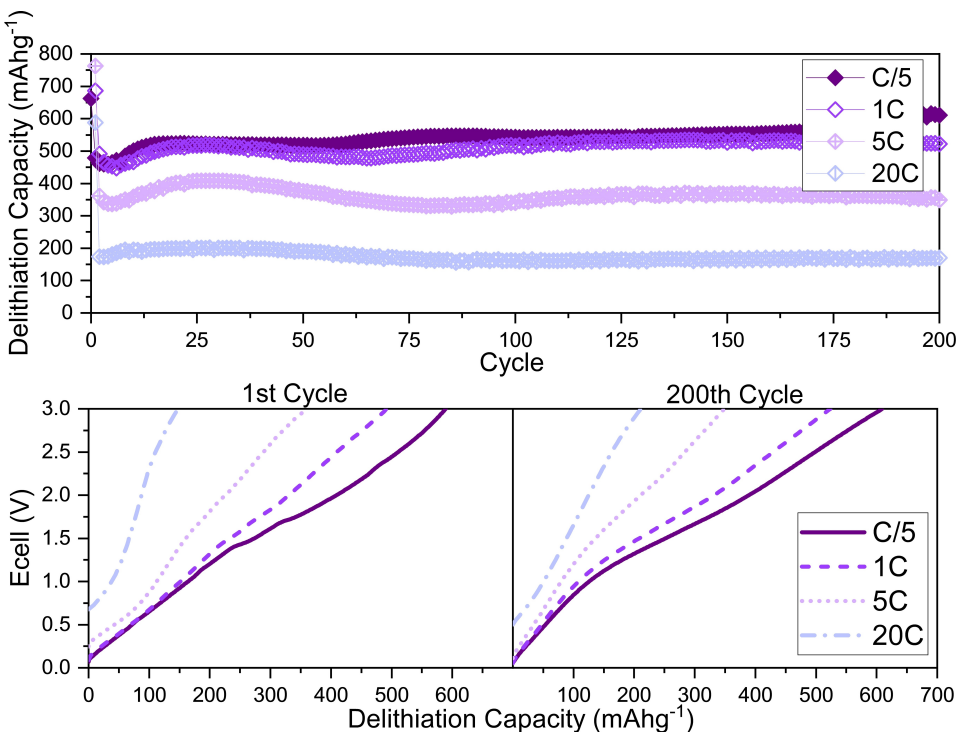


Figure 4. top) Galvanostatic cycling between 0.01–3.0 V of the $\text{Nb}_2\text{O}_5:\text{MoO}_2$ composite at various rates, (bottom) charging profiles at various rates at 1st and 200th cycle.

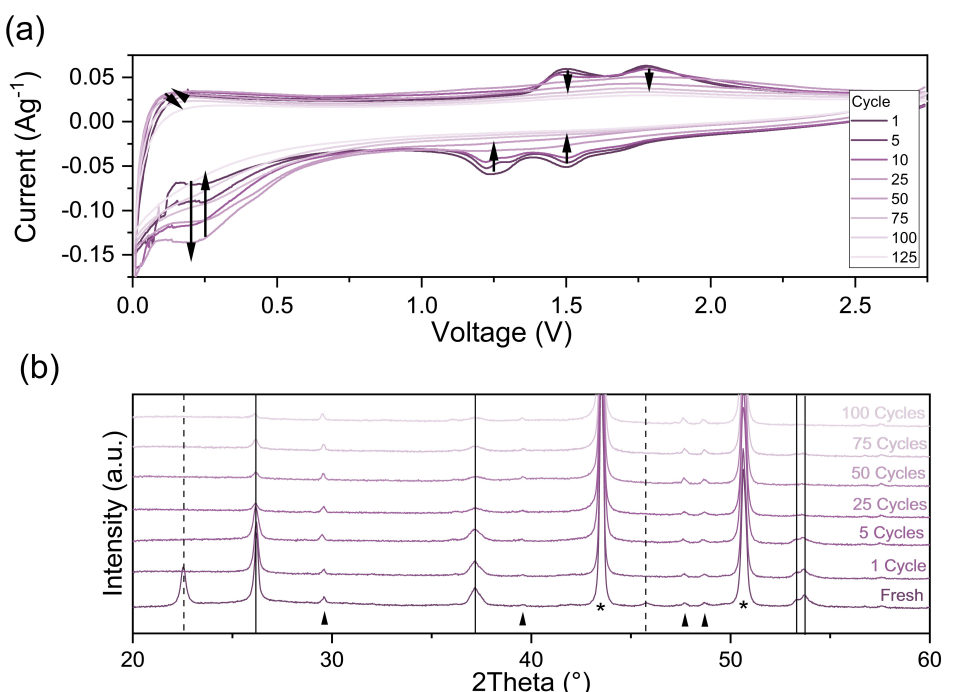


Figure 5. a) Cyclic voltammograms of the $\text{Nb}_2\text{O}_5:\text{MoO}_2$ composite at 0.1 mV s^{-1} taken between galvanostatic cycling between 1–125 cycles at 1C. b) Ex situ XRD of the $\text{Nb}_2\text{O}_5:\text{MoO}_2$ composite electrodes, fresh and cycled between 1–100 cycles at 1C in a 0.01–3.0 V voltage range. Lines denote peaks of monoclinic MoO_2 , dotted lines denote T- Nb_2O_5 peaks and * represent the peaks indexed to Cu current collector and triangles denote peaks from the sample holder.

delithiation at 0.1, 1.5 and 1.8 V. Some hysteresis in the CV profile is evident, particularly apparent in the pairs 1.25/1.5 V and 1.5/1.8 V. This may suggest that the delithiation process has a higher

activation energy compared to the lithiation process. These peaks correspond to the multi-phase Li-ion intercalation step, where the MoO₂ is known to change from monoclinic to orthorhombic to

monoclinic.^[57] Furthermore, these pairs appear to have shoulders on the peaks initially during the lithiation process, suggesting a more complex phase change than in delithiation. Peaks for this Nb_2O_5 material are typically broad and sit at 1.25 and 1.75 V and thus overlap with the MoO_2 peaks which are more apparent here for the double peak shape.^[43] The peak at 0.2 V is indicative of the conversion reaction; and grows until cycle 25 where it begins to retract. This is evidence for the increasing capacity in the first 30 cycles (Figure 4). The activation process may be linked to a structural rearrangement of MoO_2 material, which may allow for an easier conversion reaction.^[58,59] After 25 cycles, this redox peak begins to retract, suggesting that the conversion reaction is no longer taking place in full, and this may be due to an irreversible conversion causing a clustering of Mo metal, thus reducing the MoO_2 content.^[51,59,60] Alternatively, it may result from the conversion becoming unfavourable compared with other storage methods. In parallel with the activation process, the other redox peaks begin to flatten out, to the point where there appears to be one set of broad peaks in place at 1.5/1.75 V (Figure 5a). This shows a shift away from the multi-step phase change Li-ion intercalation. It is possible that following activation, the evolved MoO_2 can take on Li-ions with little change in the structure, hence a single-phase process.^[58,59] Notably, all the peaks appear to be overlaid on a broad rectangular profile. This is likely to come from the Nb_2O_5 part of this material, known for its capacitive type of response.^[12] From 60–100 cycles there appears to be a second increase in capacity (Figure 4), however, there is no obvious change in the CV profile that coincides with this (Figure 5a). As with the CV results, the ex situ XRD appears to give no

explanation to the increase in capacity at approximately 70 cycles (Figure 5b), as there is no obvious change in the XRD patterns. This capacity improvement is further probed electrochemically later.

Ex situ XRD was used to further study the Li-ion storage mechanism. Notably, after the first cycle, the crystalline peaks associated with the semi-crystalline Nb_2O_5 completely flatten (Figure S8), suggesting that the formation cycle allows a change from semi-crystalline to completely amorphous Nb_2O_5 . On the other hand, the MoO_2 Bragg peaks remain but reduce in intensity with cycling, although at 100 cycles there is still evidence of the most prominent peaks at 26° and 38°. The peaks show minimal shift with cycling and lack obvious change which suggests that the MoO_2 remains monoclinic. The impressive electrochemistry could be linked to the structural stability, as by 100 cycles there is no formation of other materials, immediate amorphisation or drastic restructuring of the material as seen in previous work on MoO_2 .^[59,61–63] Yet, this does not give an explanation to the activation process seen here, as no structural rearrangement is observed. This would suggest that the MoO_2 is stabilised in this material, and the MoO_2 particles within the stable Nb_2O_5 network is key to the improved performance.

Staircase potentiodynamic electrochemical impedance spectroscopy (SPEIS) was used to further characterise the composite electrochemically. The initial lithiation has high impedance, which is reduced as Li-ions are inserted (Figure 6). After the first cycle, the impedance is lower, even with increasing cycles. During delithiation there is an increased impedance in the range of 0.01–0.5 V, occurring in all frequency regions. This suggests resistance from

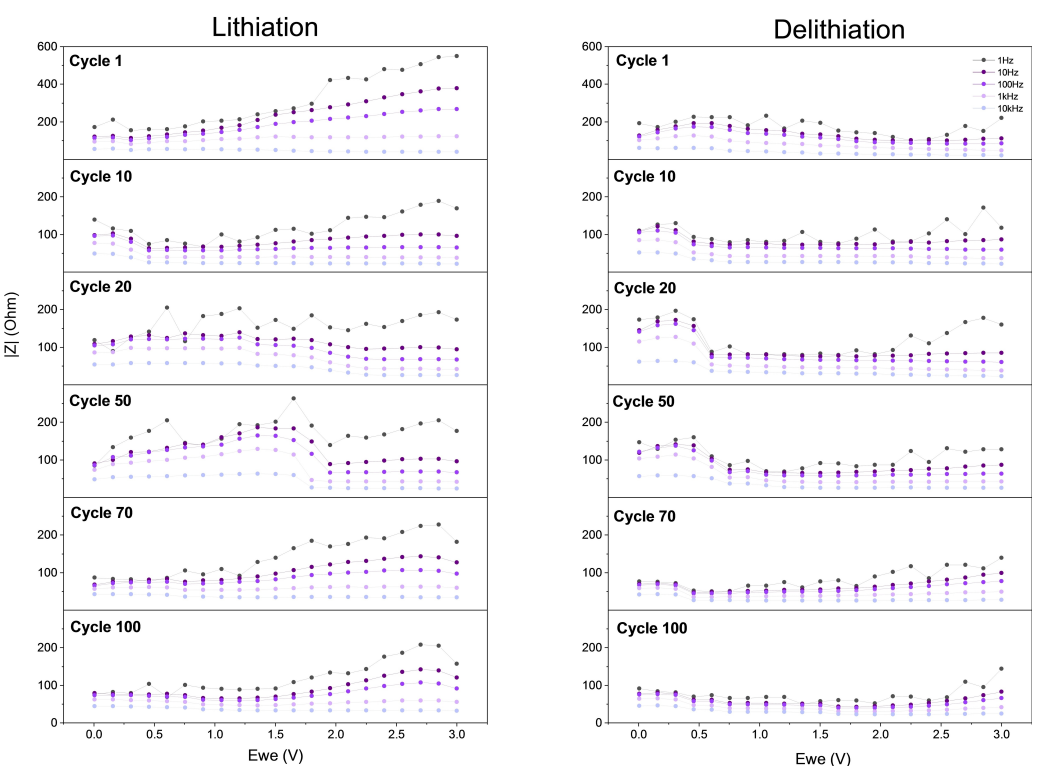


Figure 6. SPEIS profiles from the $\text{Nb}_2\text{O}_5:\text{MoO}_2$ composite for increasing cycles from 1 to 100 (top to bottom) for lithiation and delithiation (left and right respectively). Note that the y axis changes after 1 cycle.

the conversion process in MoO_2 . Interestingly, although the CV profile suggests a lack of conversion after 25 cycles, this largely continues into 50 cycles. By 70 cycles the increase in impedance between 0.01–0.5 V is reduced, and thus may link with the second increase in capacity that is seen. After 50 cycles, there is an increased impedance above 2.0 V, which suggests that with the reduction in crystallinity of MoO_2 seen after this many cycles. The charge transfer resistance also changes, likely to be due to a change in lattice expansion needed for the material to accommodate lithium.

As the composite material shows some impressive properties, especially with continued structural integrity and good capacities at higher rates (5 and 20 C), further rate testing was performed (Figure 7). As seen above there is a large step down in capacity between 5 C and 20 C, yet from 20 C to 100 C there is little change. Notably, at 50 and 100 C there is a prominent activation process seen as a large peak in capacity, which is delayed at 100 C. This feature is unusual at such a high rate as activation in MoO_2 typically requires slower rates to take place due to the demand of a structural change, typically the activation shows only a small capacity increase and takes place over many more cycles.^[51,59,63] Evidently, rate is also an important factor when considering electrochemical mechanism, as here the activation process happens in a different way to that at lower rates. Importantly, average capacities of 152 and 112 mAh g^{-1} are recorded at 200 cycles for 50 and 100 C rates respectively. These results match the capacities of Nb_2O_5 : carbon composites at high rates, whilst far surpassing them in lower rate capacity.^[52,64–66] Budak *et al.* showed an impressive capacity of 120 mAh g^{-1} at 16 A g^{-1} current density but could only reach a capacity of 250 mAh g^{-1} at a low rate of 0.05 A g^{-1} .^[52]

The charge profiles at the highest rate show notable polarisation, yet this is reduced after the activation. These profiles are almost linear, suggesting a capacitive mechanism. At this C rate it is likely that the Nb_2O_5 is the major storage material, as it is known for its intercalation pseudocapacitance.^[10,67] The high capacities suggest that the MoO_2 is key to achieving the performance, likely to be due to it contributing to a conductive network. This is supported by calculations of capacitive contribution from CV scans at increased scan rates (Figure S6). The peak current plots show a reliance on a surface limited process as the gradients are all above 0.6, where 0.5 is expected for a purely diffusion-limited process. The highest capacitive contribution is 61% at 10 mVs^{-1} , at this extent, which may suggest that capacitive storage is occurring in both oxides simultaneously, and that the composite form is key to achieving these higher rates.

Conclusion

This work has studied a novel $\text{Nb}_2\text{O}_5:\text{MoO}_2$ composite formed of an intimate mixture of Nb_2O_5 nanowires and MoO_2 nanoparticles, as prepared by a hydrothermal crystallisation and short heat-treatment. The composite achieved its theoretical capacity, as a proportionate sum of the individual oxides' theoretical values, with an average capacity of 514 mAh g^{-1} achieved even after 200 cycles at 1 C. Not only does the material provide a substantial capacity but has demonstrated an impressive performance under long-term high C-rate testing. After 400 cycles at 100 C the material is still able to achieve a specific capacity of 112 mAh g^{-1} . This excellent rate capability is likely to be due to the synergy of the high-rate Nb_2O_5 and conductive MoO_2 . The CV profiles show

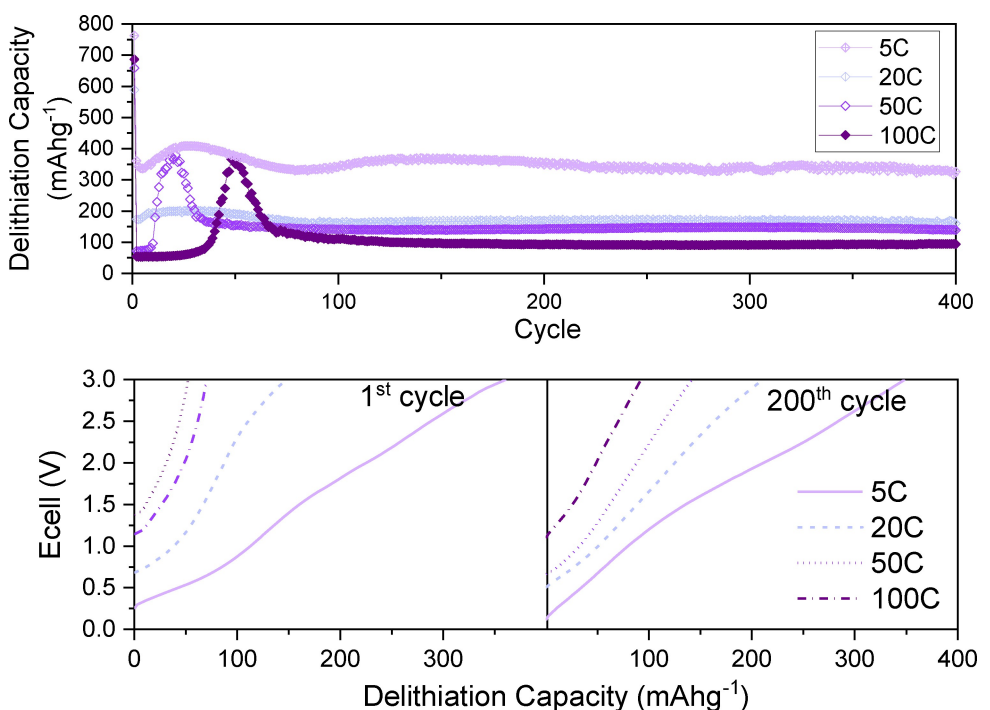


Figure 7. top) High rate galvanostatic cycling between 0.01–3.0 V of the $\text{Nb}_2\text{O}_5:\text{MoO}_2$ composite at rates greater than 5C, bottom) charging profiles at various rates at 1st and 200th cycle.

Li-ion storage using multiple methods: intercalation and conversion, and pseudocapacitive. This use of multiple-ion storage methods allows the material to produce a range of desirable electrochemical results. Unlike previous literature, the MoO₂ in the composite appears to have structural stability as seen via ex situ XRD upon cycling, which helps to further provide cycle stability. The material shows high rate results comparable to the high rate Nb₂O₅:carbon composites, yet gives much higher capacities than could be achieved at low rates. Equally, the material's rate capability and stability would be hard to match by a conventional MoO₂ material. The composite offers a significant advantage of operating at a higher cycling rate: the properties are greater than the sum of its parts. This may make it highly suited for specific applications, such as in transport applications and devices requiring fast charge.

Experimental Section

The synthesis of Nb₂O₅ was explored in our previous work,^[43] and the optimised method has been adapted here to produce a Nb₂O₅:MoO₂ composite with a 50:50 molar ratio of the metal containing precursors. 2.85 mmol ammonium molybdate tetrahydrate, (NH₄)₆Mo₇O₂₄·4H₂O, (Sigma Aldrich, 99.98%) and 20 mmol ammonium niobate oxalate hydrate, NbO(C₂O₄)₂(NH₄)·5H₂O, (Sigma Aldrich, 99.99%) were dissolved in 30 mL of 10% w/v oxalic acid in deionised water and charged into a 125 mL Teflon liner, within a steel autoclave. The hydrothermal synthesis was conducted at 225 °C for 72 h within a fan oven. The solid product was separated via centrifugation, washed with deionised water (3 × 100 mL) and dried at 70 °C for 24 h. Heat-treatment of the as-synthesised composite in a tube furnace (Carbolite, Gero), at 600 °C in Ar (~5 mL min⁻¹) was used to produce the final composite material.

Powder X-ray diffraction (XRD) patterns were collected using a Panalytical Empyrean diffractometer (Cu K $\alpha_{1/2}$ source) scanned from 10° to 90°, with a 30 min scan time. Powders were dusted onto adhesive carbon tabs on stubs for scanning electron microscopy (SEM) imaging using a JEOL 7800F microscope. SEM-energy dispersive X-ray (EDX) spectroscopy, (AZtec software, Oxford Instruments) mapping was performed using a 3-minute scan time and a 1080p resolution to produce coloured SEM-EDX maps. For transmission electron microscopy (TEM) (FEI Talos), the powders were ultrasonically dispersed in methanol at a concentration of 1 mg mL⁻¹. 20 μ L of this dispersion was pipetted onto Cu grids coated with holey carbon films (Agar Scientific), placed on filter paper and then allowed to dry under ambient conditions. Scanning transmission electron microscopy (STEM) imaging and STEM-EDX was completed on the same sample set up with the same instrument. X-ray fluorescence (XRF) (Rigaku Primus IV wavelength dispersive XRF) spectroscopy was used to confirm the ratios of metal atoms in the composite materials. Samples were loaded on FluXana sample holders, covered with a Kapton film, and the data were compared to internal standards to identify the atomic composition. The XPS data were collected and analysed using a Kratos Axis Ultra DLD spectrometer, where samples investigated were attached to electrically conductive carbon tape. The spectra were analysed in the CasaXPS package using Shirley backgrounds.^[68] Mixed Gaussian-Lorentzian (Voigt) line shapes were used to analyse all regions except for the Mo 3d region. Here, in samples which exhibited screened and unscreened Mo (IV) states, an asymmetric Voigt (GL(20)T(1.5)) was used for the Mo(IV) screened components, while a modified asymmetric Lorentzian line shape (LF(1,1,35,280)) was used for the Mo(IV) unscreened and Mo(VI) components.

Anode coatings were produced by the co-dispersion of active materials with conductive carbon black (C65, Timcal) and PVDF (8% w/v solution in 1-methylpyrrolidin-2-one (NMP)), in a ratio of 70:20:10% w/w (active material: carbon: binder). Firstly, the active material and C65 were ground using a pestle and mortar then dispersed in NMP using an ultra-sonication probe (2 × 5 min), before the PVDF solution was added. The slurry was mixed (THINKY MIXER ARE-250) at 2000 rpm (4 × 5 min). The slurry was cast onto copper foil using a doctor blade at 50 μ m blade gap and the electrode was subsequently dried in air at 80 °C with further vacuum drying at 40 °C for an hour, resulting in electrode loadings of 0.75 ± 0.05 mg cm⁻². Half cells were produced in an Ar filled glove box (Inert, Pure Lab HE) by positioning anodes against metallic lithium foil, incorporating a separator in between with electrolyte (1.0 M LiPF₆ in 3/7 v/v ethylene carbonate: ethyl methyl carbonate with 1% w/v vinylene carbonate (Soulbrain, PuriEL)). For coin cells, a Celgard 2325 separator is used, and the cells were used for galvanostatic cycling, rate testing and electrochemical impedance spectroscopy (EIS) measurements. Swagelok cells used glass fibre separators (Whatman) and were used for cyclic voltammetry (CV) testing. All cells underwent an 8-hour open circuit voltage step prior to testing. Galvanostatic cycling (BioLogic BCS potentiostat) used a 0.01–3.0 V window and a single formation cycle at C/20, all lithiation steps had a 3-hour potential hold at all rates, where the delithiation used no potential hold. Staircase potential EIS (SPEIS) (BioLogic VMP3 potentiostat) was measured in a 10 kHz to 1 Hz frequency range. Cyclic voltammetry (CV) (BioLogic VMP3 potentiostat) was taken at 0.5 mV s⁻¹ after every 5 cycles at 1 C. Testing at increasing scan rates of 1, 2, 3, 4, 5, 10, 20, 25, 30, 40, 50, 60, 70, 75, 80, 90 and 100 mV s⁻¹ for a single cycle at each rate was analysed via the Dunn method.^[69]

Acknowledgements

The authors would like to thank the UKRI, EPSRC and ERA for funding this study via the studentship EP/N509796/1. We thank the Faraday Institution SafeBatt project (FIRG028) and the High Value Manufacturing Catapult for funding facilities at the Energy Innovation Centre, WMG at the University of Warwick. We are grateful to Geoff West, Fengzai Tang, Sabrina Yan and Tom Moore from the microscopy facility at WMG for experiment assistance, and David Walker and Steve Huband at the X-ray Research Technology Platform at Warwick for their help with further experimental work. We thank Marc Walker for collection and analysis of XPS data from the Photoemission Research Technology Platform, University of Warwick.

Conflict of Interest

The authors declare no conflict of interest.

Keywords: anode · composite · lithium storage · molybdenum oxide · niobium oxide

- [1] M. V. Reddy, G. V. Subba Rao, B. V. R. Chowdari, *Chem. Rev.* **2013**, *113*, 5364–5457.
- [2] S. Boyd, V. Augustyn, *Inorg. Chem. Front.* **2018**, *5*, 999–1015.
- [3] C. Dong, W. Dong, X. Lin, Y. Zhao, R. Li, F. Huang, *EnergyChem* **2020**, *2*, 100045.

- [4] R. S. Devan, R. A. Patil, J. H. Lin, Y. R. Ma, *Adv. Funct. Mater.* **2012**, *22*, 3326–3370.
- [5] C.-Q. Yi, J.-P. Zou, H.-Z. Yang, X. Leng, *Trans. Nonferrous Met. Soc. China* **2018**, *28*, 1980–2001.
- [6] J. B. Goodenough, *Chem. Mater.* **2014**, *26*, 820–829.
- [7] P. Poizot, S. Laruelle, S. Grugeon, L. Dupont, J. Tarascon, *Nature* **2000**, *407*, 496–499.
- [8] J. B. Goodenough, *Prog. Solid State Chem.* **1971**, *5*, 145–399.
- [9] M. Lübbe, A. Sumboja, I. D. Johnson, D. J. L. Brett, P. R. Shearing, Z. Liu, J. A. Darr, *Electrochim. Acta* **2016**, *192*, 363–369.
- [10] J. W. Kim, V. Augustyn, B. Dunn, *Adv. Energy Mater.* **2012**, *2*, 141–148.
- [11] K. Brezesinski, J. Wang, J. Haetge, C. Reitz, S. O. Steinmueller, S. H. Tolbert, B. M. Smarsly, B. Dunn, T. Brezesinski, *J. Am. Chem. Soc.* **2010**, *132*, 6982–6990.
- [12] V. Augustyn, P. Simon, B. Dunn, *Energy Environ. Sci.* **2014**, *7*, 1597.
- [13] M. Winter, R. J. Brodd, *Chem. Rev.* **2004**, *104*, 4245–4269.
- [14] N. A. Chernova, M. Roppolo, A. C. Dillon, M. S. Whittingham, *J. Mater. Chem.* **2009**, *19*, 2526.
- [15] N. Kumagai, K. Tanno, T. Nakajima, N. Watanabe, *Electrochim. Acta* **1983**, *28*, 17–22.
- [16] T. Ohzuku, K. Sawai, T. Hirai, *J. Power Sources* **1987**, *19*, 287–299.
- [17] C. P. Koçer, K. J. Griffith, C. P. Grey, A. J. Morris, *Phys. Rev. B* **2019**, *99*, 1–11.
- [18] T. Qin, Q. Wang, D. Yue, H. Liu, Y. Zheng, Y. Han, C. Gao, *J. Alloys Compd.* **2020**, *814*, 152336.
- [19] D. B. Rogers, R. D. Shannon, A. W. Sleight, J. L. Gillson, *Inorg. Chem.* **1969**, *8*, 841–849.
- [20] K. Tang, S. A. Farooqi, X. Wang, C. Yan, *ChemSusChem* **2019**, *12*, 755–771.
- [21] A. Kim, E. Park, H. Lee, H. Kim, *J. Alloys Compd.* **2016**, *681*, 301–306.
- [22] W. Wang, F. Xiong, S. Zhu, J. Chen, J. Xie, Q. An, *eScience* **2022**, *2*, 278–294.
- [23] Q. Deng, Y. Fu, C. Zhu, Y. Yu, *Small* **2019**, *15*, 1–26.
- [24] H. Ding, Z. Song, H. Zhang, X. Li, *Mater. Today Nano* **2020**, *11*, 100082.
- [25] J. Liao, W. Ni, C. Wang, J. Ma, *Chem. Eng. J.* **2020**, *391*, 123489.
- [26] W. Tang, C. X. Peng, C. T. Nai, J. Su, Y. P. Liu, M. V. V. Reddy, M. Lin, K. P. Loh, *Small* **2015**, *11*, 2446–2453.
- [27] C. Xia, Y. Zhou, D. B. Velusamy, A. A. Farah, P. Li, Q. Jiang, I. N. Odeh, Z. Wang, X. Zhang, H. N. Alshareef, *Nano Lett.* **2018**, *18*, 1506–1515.
- [28] Y. Yun, Z. Shi, J. Shao, Q. Qu, Y. Gao, Z. Chen, Y. Chen, H. Zheng, *ChemNanoMat* **2018**, *4*, 1247–1253.
- [29] C. Kim, H. J. Cho, K. R. Yoon, J. Y. Cheong, S. H. Cho, J. W. Jung, S. W. Song, I. D. Kim, *ACS Appl. Mater. Interfaces* **2021**, *13*, 587–596.
- [30] S. Deng, H. Zhu, G. Wang, M. Luo, S. Shen, C. Ai, L. Yang, S. Lin, Q. Zhang, L. Gu, B. Liu, Y. Zhang, Q. Liu, G. Pan, Q. Xiong, X. Wang, X. Xia, J. Tu, *Nat. Commun.* **2020**, *11*, 132.
- [31] H. Li, H. Zhou, *Chem. Commun.* **2012**, *48*, 1201–1217.
- [32] H. J. Zhang, K. X. Wang, X. Y. Wu, Y. M. Jiang, Y. B. Zhai, C. Wang, X. Wei, J. S. Chen, *Adv. Funct. Mater.* **2014**, *24*, 3399–3404.
- [33] W. Devina, J. Hwang, J. Kim, *Chem. Eng. J.* **2018**, *345*, 1–12.
- [34] J. Liu, S. Tang, Y. Lu, G. Cai, S. Liang, W. Wang, X. Chen, *Energy Environ. Sci.* **2013**, *6*, 2691–2697.
- [35] T. Stephenson, Z. Li, B. Olsen, D. Mitlin, *Energy Environ. Sci.* **2014**, *7*, 209–231.
- [36] Z. Xu, T. Wang, L. Kong, K. Yao, H. Fu, K. Li, L. Cao, J. Huang, Q. Zhang, *Part. Part. Syst. Charact.* **2017**, *34*, 1600223.
- [37] Z. Xu, H. Wang, Z. Li, A. Kohandehghan, J. Ding, J. Chen, K. Cui, D. Mitlin, *J. Phys. Chem. C* **2014**, *118*, 18387–18396.
- [38] D. Cao, Z. Yao, J. Liu, J. Zhang, C. Li, *Energy Storage Mater.* **2018**, *11*, 152–160.
- [39] H. Park, D. Lee, T. Song, *J. Power Sources* **2019**, *414*, 377–382.
- [40] G. Li, X. Wang, Z. Chen, X. Ma, Y. Lu, *Electrochim. Acta* **2013**, *102*, 351–357.
- [41] K. Kim, J. H. Kim, *J. Mater. Chem. A* **2018**, *6*, 13321–13330.
- [42] W. Wang, G. Shi, H. Cai, C. Zhao, J. Wu, Y. Yu, J. Hu, Z. Fang, J. Yan, B. Liu, *J. Alloys Compd.* **2019**, *792*, 191–202.
- [43] E. C. Wheeler-Jones, M. J. Loveridge, R. I. Walton, *Electrochim. Acta* **2021**, *392*, 138964.
- [44] C. Nico, T. Monteiro, M. P. F. Graça, *Prog. Mater. Sci.* **2016**, *80*, 1–37.
- [45] C. Zener, *J. Appl. Phys.* **1949**, *20*, 950–953.
- [46] L. A. ODell, S. L. P. Savin, A. V. Chadwick, M. E. Smith, *J. Phys. Chem. C* **2007**, *111*, 13740–13746.
- [47] S. C. Chen, M. Greenblatt, *J. Solid State Chem.* **1994**, *108*, 366–370.
- [48] B. M. Gatehouse, A. D. Wadsley, *Acta Crystallogr.* **1964**, *17*, 1545–1554.
- [49] B. G. Brandt, A. C. Skapski, E. Thom, E. Stoll, G. Eriksson, R. Blinc, S. Paušák, L. Ehrenberg, J. Dumanović, *Acta Chem. Scand.* **1967**, *21*, 661–672.
- [50] V. V. Atuchin, I. E. Kalabin, V. G. Kesler, N. V. Pervukhina, *J. Electron Spectrosc. Relat. Phenom.* **2005**, *142*, 129–134.
- [51] B. Guo, X. Fang, B. Li, Y. Shi, C. Ouyang, Y. S. Hu, Z. Wang, G. D. Stucky, L. Chen, *Chem. Mater.* **2012**, *24*, 457–463.
- [52] Ö. Budak, M. Geißler, D. Becker, A. Kruth, A. Quade, R. Haberkorn, G. Kickelbick, B. J. M. Etzold, V. Presser, *ACS Appl. Energ. Mater.* **2020**, *3*, 4275–4285.
- [53] X. Liu, J. Yang, W. Hou, J. Wang, Y. Nuli, *ChemSusChem* **2015**, *8*, 2621–2624.
- [54] Z. Hu, Q. He, Z. Liu, X. Liu, M. Qin, B. Wen, W. Shi, Y. Zhao, Q. Li, L. Mai, *Sci. Bull. (Beijing)* **2020**, *65*, 1154–1162.
- [55] H. Ding, Z. Song, K. Feng, H. Zhang, H. Zhang, X. Li, *J. Solid State Chem.* **2021**, *299*, 122136.
- [56] W. Zhang, P. Shen, L. Qian, Y. Wang, H. Arandiyani, H. Mahmoud, X. Liu, J. Wang, X. Wang, Y. Liu, H. Sun, Y. Yu, *ACS Appl. Energ. Mater.* **2021**, *4*, 4551–4560.
- [57] J. R. Dahn, W. R. McKinnon, *Solid State Ionics* **1987**, *23*, 1–7.
- [58] J. H. Ku, Y. S. Jung, K. T. Lee, C. H. Kim, S. M. Oh, *J. Electrochem. Soc.* **2009**, *156*, A688.
- [59] H. J. Zhang, J. Shu, K. X. Wang, X. T. Chen, Y. M. Jiang, X. Wei, J. S. Chen, *J. Mater. Chem. A* **2014**, *2*, 80–86.
- [60] S. Petnikota, K. W. Teo, L. Chen, A. Sim, S. K. Marka, M. V. Reddy, V. V. S. S. Srikanth, S. Adams, B. V. R. Chowdari, *ACS Appl. Mater. Interfaces* **2016**, *8*, 10884–10896.
- [61] J. H. Ku, J. H. Ryu, S. H. Kim, O. H. Han, S. M. Oh, *Adv. Funct. Mater.* **2012**, *22*, 3658–3664.
- [62] A. Manthiram, *J. Electrochem. Soc.* **1996**, *143*, L143.
- [63] Y. Liang, S. Yang, Z. Yi, J. Sun, Y. Zhou, *Mater. Chem. Phys.* **2005**, *93*, 395–398.
- [64] S. Fu, Q. Yu, Z. Liu, P. Hu, Q. Chen, S. Feng, L. Mai, L. Zhou, *J. Mater. Chem. A* **2019**, *7*, 11234–11240.
- [65] Y. Lian, D. Wang, S. Hou, C. Ban, J. Zhao, H. Zhang, *Electrochim. Acta* **2020**, *330*, 135204.
- [66] Z. Song, H. Li, W. Liu, H. H. Zhang, J. Yan, Y. Tang, J. Huang, H. H. Zhang, X. Li, *Adv. Mater.* **2020**, *32*, 1–9.
- [67] J. Come, V. Augustyn, J. W. Kim, P. Rozier, P.-L. Taberna, P. Gogotsi, J. W. Long, B. Dunn, P. Simon, *J. Electrochem. Soc.* **2014**, *161*, A718–A725.
- [68] N. Fairley, V. Fernandez, M. Richard-Plouet, C. Guillot-Deudon, J. Walton, E. Smith, D. Flahaut, M. Greiner, M. Biesinger, S. Tougaard, D. Morgan, J. Baltrusaitis, *Appl. Surf. Sci.* **2021**, *5*, 100112.
- [69] V. Augustyn, J. Come, M. A. Lowe, J. W. Kim, P. L. Taberna, S. H. Tolbert, H. D. Abruña, P. Simon, B. Dunn, *Nat. Mater.* **2013**, *12*, 518–522.

Manuscript received: December 21, 2022

Revised manuscript received: March 10, 2023

Accepted manuscript online: March 13, 2023

Version of record online: March 27, 2023